Preprints of the 21st IFAC World Congress (Virtual)
Berlin, Germany, July 12-17, 2020

Sensing and Decentralized Control of a Five-Axis Monolithic Nanopositioning Stage

Meysam Omidbeike* Yuen K. Yong* Andrew. J. Fleming*

* *Precision Mechatronics Lab, The University of Newcastle,Callaghan, NSW, 2308, Australia(e-mail: Meysam.Omidbeike@newcastle.edu.au).*

Abstract: This article describes the design and calibration of a five degree-of-freedom linear and angular displacement sensor utilizing piezoresistive strain gages. A simple decentralized controller is then implemented to follow linear and angular reference signals. The foremost difficulty with piezoresistive sensors is their high-temperature sensitivity. In addition, they are sensitive to motion in multiple degrees of freedom, which must be decoupled before use as a displacement sensor. A new sensing design is proposed which provides decoupled measurements of linear and angular displacements in multi-axis monolithic nanopositioning stages. The proposed method employs system identification and feedforward techniques to calibrate each axis and minimize cross-coupling.

Keywords: Nanopositioning, Piezoresistive sensors, Decentralized control

1. INTRODUCTION

Nanopositioners are electro-mechanical devices capable of generating high-resolution motion in up to six degrees of freedom (DOF) (Fleming and Leang (2014)). Common nanopositioning applications include scanning probe microscopy (Ruppert et al. (2019)), lithography (Ghalehbeygi et al. (2017)), and nanofabrication (Gates et al. (2004)).

In this paper, a new monolithic nanopositioner is introduced (Fleming and Yong (2017)). Parallel actuators driving a central platform are etched into a bimorph piezoelectric sheet to provide both actuation and guidance of the moving platform (Moore et al. (2018); Omidbeike et al. (2017)). The actuator configuration for this stage yields five DOF. The stage, mounted on an insulated base, is shown in Fig. 1. Details on the design and manufacturing process can be found in Fleming and Yong (2017) and Omidbeike et al. (2019).

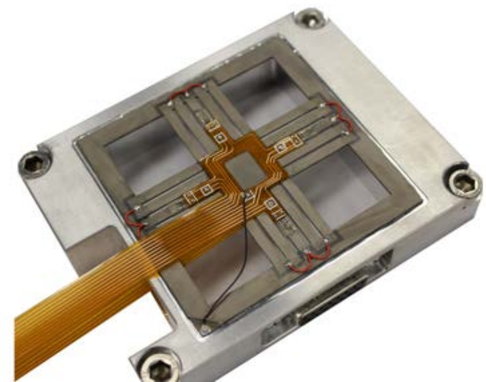

Fig. 1. Monolithic bimorph nanopositioner mounted on a base.

The sensor requirements of a nanopositioning system are among the most demanding of any control system (Fleming and Leang (2014)). Among the various types of sensing techniques available in the literature, capacitive sensing (Moore et al. (2019)), piezoelectric sensing (Omidbeike et al. (2017)), piezoresistive sensing (Omidbeike et al. (2018)) and optical type sensors (Fleming and Routley (2015)), can be identified as the most common types available. Each of these sensors has its own advantages and disadvantages based on their applications.

Due to their high sensitivity and low noise, piezoresistive sensors have been widely used in nanopositioning applications (Fleming and Leang (2014)). As a displacement sensor, piezoresistive sensors are mostly employed for the measurement of only a single variable, i.e. either rotation or linear displacement but not both. Examples include piezoresistive strain sensor embedded in the atomic force microscopy (AFM) cantilever introduced in Tortonese et al. (1993) and linear displacement measurement in nanopositioning systems proposed in Sun et al. (2008). For the simultaneous measurement of several displacements and rotation angles, various sensors utilizing capacitive or optical sensing schemes have been introduced including Anandan and George (2017) and Sommargren (1989).

The foremost difficulty with piezoresistive sensors is the high-temperature sensitivity of both the total resistance and gage factor. The Wheatstone-bridge discussed in Ekelof (2001) is the most common configuration for temperature compensation in strain gage sensors. However, this method can only be used for a single axis displacement measurement where equal and opposite strain is available.

This article presents a five-DOF linear and angular displacement sensor instrumented with a set of eight piezoresistive sensors. The eight sensors are configured in a way which naturally provides temperature stability for all

Copyright lies with the authors

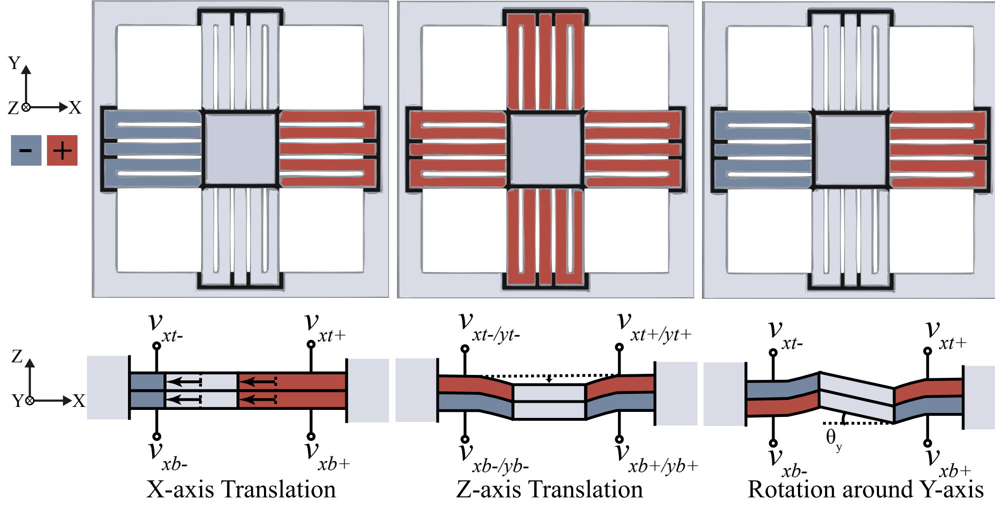

Fig. 2. The five-axis motions generated with different applied voltages.

five degrees-of-freedom. System identification methods are then used to calibrate the sensors and minimize error due to cross-coupling.

2. MONOLITHIC NANOPOSITIONER

The design and manufacturing process of the nanopositioning stage used in this work is the same as the monolithic stage described in Fleming and Yong (2017) but here a bimorph piezoelectric sheet is used to provide out-of-plane displacement (z-axis) and rotation around the X and Y axis. The nanopositioning stage is mounted on an insulating base as shown in Fig. 1. An analysis of the design is reported in Omidbeike et al. (2019).

The five-axis motions generated from different applied voltages are shown in Fig. 2. Each piezoelectric layer is outwardly poled. With the middle layer grounded, a positive voltage applied to the top and bottom electrodes will cause the beam to expand and displace the central platform away from the positive voltage. For example, when a positive voltage is applied to v_{xt+} and v_{xb+}, and an equal and opposite voltage is applied to v_{xt-} and v_{xb-}, the central platform will translate in the negative X-direction.

The stage has 8 inputs and 5 outputs, where the inputs are the applied voltages to the top and bottom electrodes and the outputs are the translations along the X, Y and Z axes and the rotations about the X and Y axes. The electrode voltages can be grouped to correspond to the three translations and two rotations. This is done by creating a transformation matrix that maps the five inputs to the eight electrode voltages. Using this transformation, the system is square with five inputs and five outputs. The inputs are $u_x, u_y, u_z, u_{\theta_x}$ and u_{θ_y} and the outputs are the translations d_x, d_y and d_z and rotations θ_x and θ_y.

2.1 Transformation Matrix (Jacobian)

The transformation matrix is denoted $\mathbf{J}$, and maps the five inputs

$$\mathbf{u} = [u_x \, u_y \, u_z \, u_{\theta_x} \, u_{\theta_y}]^{\mathrm{T}}$$

to the eight physical electrode voltages

$$\mathbf{v} = [v_{xt+} \, v_{xb+} \, v_{xt-} \, v_{xb-} \, v_{yt+} \, v_{yb+} \, v_{yt-} \, v_{yb-}]^{\mathrm{T}}$$

using the expression $\mathbf{v} = \mathbf{Ju}$. The transformation matrix $\mathbf{J}$ encodes how the inputs $\mathbf{u}$ generates motion via the electrode voltages $\mathbf{v}$. For example, the first column of $\mathbf{J}$ corresponds to translation along the X-axis where the top and bottom actuators on each side are driven with equal and opposite voltages. Therefore, electrodes for the motion in the X-axis are selected by using elements ± 1, where the sign is determined by the required polarity of the applied voltage. Similarly, selecting the electrodes using elements ± 1 according to which motions are desired, the transformation from $\mathbf{u}$ to $\mathbf{v}$ can be constructed as

$$\begin{bmatrix} v_{xt+} \\ v_{xb+} \\ v_{xt-} \\ v_{xb-} \\ v_{yt+} \\ v_{yb+} \\ v_{yt-} \\ v_{yb-} \end{bmatrix} = \begin{bmatrix} 1 & 0 & 1 & 0 & 1 \\ 1 & 0 & -1 & 0 & -1 \\ -1 & 0 & 1 & 0 & -1 \\ -1 & 0 & -1 & 0 & 1 \\ 0 & 1 & 1 & 1 & 0 \\ 0 & 1 & -1 & -1 & 0 \\ 0 & -1 & 1 & -1 & 0 \\ 0 & -1 & -1 & 1 & 1 \end{bmatrix} \begin{bmatrix} u_x \\ u_y \\ u_z \\ u_{\theta_x} \\ u_{\theta_y} \end{bmatrix}. \quad (1)$$

The naming convention used for the electrode voltages $\mathbf{v}$ is according to Fig. 2, where the subscript denotes the direction and layer. The product $\mathbf{Ju}$ is

$$\begin{bmatrix} v_{xt+} \\ v_{xb+} \\ v_{xt-} \\ v_{xb-} \\ v_{yt+} \\ v_{yb+} \\ v_{yt-} \\ v_{yb-} \end{bmatrix} = \begin{bmatrix} u_x + u_z + u_{\theta_y} \\ u_x - u_z - u_{\theta_y} \\ -u_x + u_z - u_{\theta_y} \\ -u_x - u_z + u_{\theta_y} \\ u_y + u_z + u_{\theta_x} \\ u_y - u_z - u_{\theta_x} \\ u_y + u_z - u_{\theta_x} \\ u_y - u_z + u_{\theta_x} \end{bmatrix}. \quad (2)$$

Considering equation (1), it can be seen that $\mathbf{J}$ is the Jacobian matrix of the right hand side of equation (2).

3. SENSOR CONFIGURATION AND CALIBRATION PROCESS

3.1 Sensor Configuration

Fig. 3 shows the proposed piezoresistive sensing configuration for displacement measurement in five DOF. The translational and rotational motions can be estimated

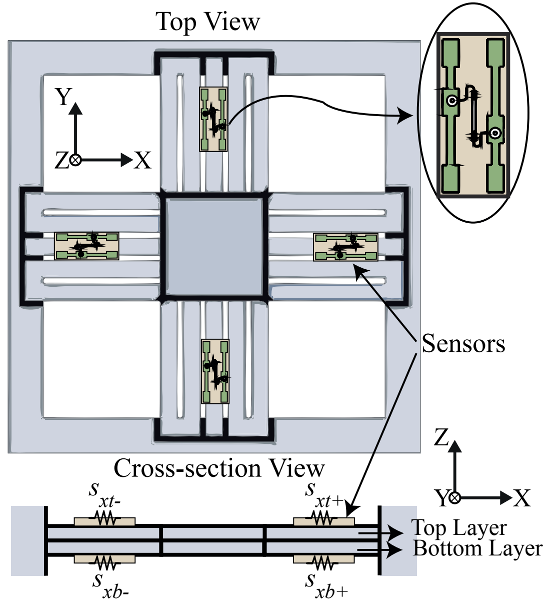

Fig. 3. Bar shaped Piezoresistive sensors mounted on the top and bottom surfaces of the middle flexures located on four sides of the nanopositioner.

from the output of eight piezoresistive sensors bonded to the top and bottom surfaces of the middle electrodes. The piezoresistive sensors used in this design are bar-shaped semiconductor gages from the Micron Instruments. For an optimum sensor output, piezoresistive sensors are placed at positions where maximum strain is presented. The sensor locations were chosen based on a finite element analysis (FEA) to maximize sensitivity to the desired strain.

To measure the surface strain, each piezoresistive sensor is connected to a circuit capable of measuring resistance change corresponding to strain. The circuit diagram of the piezoresistive strain measurement is shown in Fig. 4. The circuit output voltage measured between the middle node of the voltage divider is a function of the sensor resistance and therefore proportional to the applied strain.

3.2 Temperature Compensation

The foremost difficulty associated with piezoresistive sensors is the high temperature dependency of both the total resistance and gage factor. The differential measurement from a Wheatstone-bridge is the most common temperature compensation technique for strain gage sensors. To create a differential measurement similar to that of a Wheatstone bridge, a thermal stability matrix forcing differential measurement is created. As sensors are at the same temperature and mounted on the same material, any changes in temperature will affect the measured voltages in the same way. Therefore, differential measurement of the sensor voltages will cancel the effect of the temperature variation. This can be done using a matrix that maps the eight sensor voltages

$$\mathbf{v_s} = [v_{s_{xt+}}\, v_{s_{xb+}}\, v_{s_{xt-}}\, v_{s_{xb-}}\, v_{s_{yt+}}\, v_{s_{yb+}}\, v_{s_{yt-}}\, v_{s_{yb-}}]^{\mathrm{T}}$$

to the five outputs which are the displacement voltages

$$\mathbf{v_t} = [v_x, v_y, v_z, v_{\theta_x}, v_{\theta_y}]^{\mathrm{T}}$$

using the expression $\mathbf{v_s} = \mathbf{T_v}\mathbf{v_t}$. The naming convention used for the sensor voltages in $\mathbf{v_s}$ is according to Fig. 3,

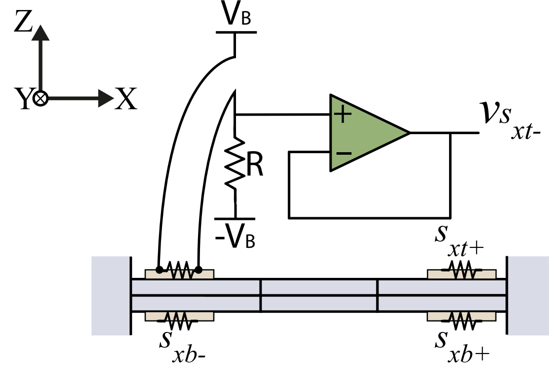

Fig. 4. Circuit diagram of the piezoresistive strain measurement.

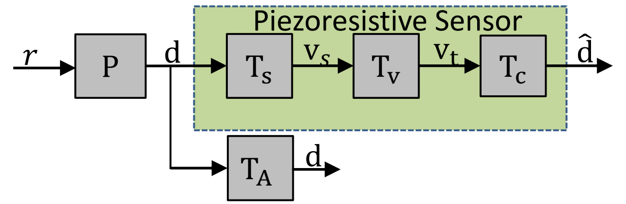

Fig. 5. The signal processing chain of the sensor calibration. $\mathbf{P}$ is the nanopositioner, $\mathbf{T_s}$ is the sensor matrix, $\mathbf{T_v}$ is the thermal stability matrix, $\mathbf{T_c}$ is the calibration matrix and $\mathbf{T_A}$ is the calibration sensor.

where the subscript denotes the sensor location in the XY plane and layer. The thermal stability matrix $\mathbf{T_v}$ encodes the information of which sensors should be used for strain measurement with temperature compensation in each axis. For example, sensors for the displacement in the X-axis are selected by using elements ± 1, where the sign is determined by the polarity of the sensor voltage to force differential measurement. Similarly, selecting the sensors using elements ± 1 according to the displacement axis, the transformation from $\mathbf{v_s}$ to $\mathbf{v_t}$ is constructed as

$$\begin{bmatrix} v_x \\ v_y \\ v_z \\ v_{\theta_x} \\ v_{\theta_y} \end{bmatrix} = \begin{bmatrix} 1 & 1 & -1 & -1 & 0 & 0 & 0 & 0 \\ 0 & 0 & 0 & 0 & 1 & 1 & -1 & -1 \\ 1 & -1 & 1 & -1 & 1 & -1 & 1 & -1 \\ 0 & 0 & 0 & 0 & 1 & -1 & 1 & -1 \\ 1 & -1 & 1 & -1 & 0 & 0 & 0 & 0 \end{bmatrix} \begin{bmatrix} v_{s_{xt+}} \\ v_{s_{xb+}} \\ v_{s_{xt-}} \\ v_{s_{xb-}} \\ v_{s_{yt+}} \\ v_{s_{yb+}} \\ v_{s_{yt-}} \\ v_{s_{yb-}} \end{bmatrix}. \quad (3)$$

Note that the thermal stability matrix $\mathbf{T_v}$ is a transpose of $\mathbf{J}$ described in Section 2.1.

3.3 Calibration Process

The signal processing chain of the sensor is shown in Fig. 5. Here, $\mathbf{P}$ is the monolithic nanopositioner, $\mathbf{T_A}$ is the Attocube laser interferometer used as a calibration device, $\mathbf{T_s}$ is the sensor matrix with eight output voltages, $\mathbf{T_v}$ is the thermal stability matrix and $\mathbf{T_c}$ is the calibration matrix. Our objective is to identify $\mathbf{T_c}$, based on matrices $\mathbf{T_s}$ and $\mathbf{T_v}$ to minimize the error

$$e = \mathbf{d} - \widehat{\mathbf{d}}, \quad (4)$$

where $\mathbf{d}$ is the true displacement measured from the calibration device and $\widehat{\mathbf{d}}$ is the estimated displacement.

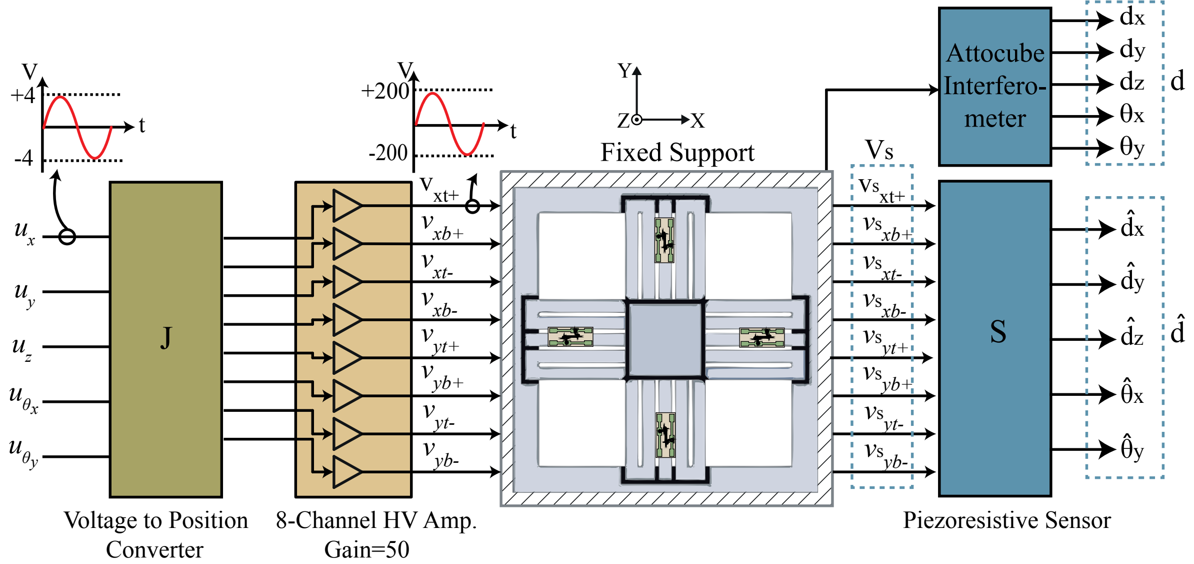

Fig. 6. Experimental configuration of the monolithic nanopositioner.

The equation relating the estimated displacement vector $\widehat{\mathbf{d}}$ to the true displacement $\mathbf{d}$ can be written as,

$$\widehat{\mathbf{d}} = \mathbf{T_c T_v T_s d}. \tag{5}$$

The objective is to find a matrix $\mathbf{T_c}$ that makes $\widehat{\mathbf{d}} = \mathbf{d}$ therefore,

$$\mathbb{I}_\mathbf{n} = \mathbf{T_c T_v T_s}. \tag{6}$$

Matrix $\mathbf{T_v}$ is already found in Section 3.2 therefore by identifying $\mathbf{T_s}$, the calibration matrix $\mathbf{T_c}$ can be identified from

$$\mathbf{T_c} = (\mathbf{T_v T_s})^{-1}. \tag{7}$$

To identify $\mathbf{T}_\mathrm{s}$ from measurements of $\mathbf{d}$ and $\mathbf{v_s}$, consider a general case for a sensor with n inputs and m outputs

$$\mathbf{T}_\mathrm{s} \in \mathbb{R}^{m\times n}, \mathbf{d} \in \mathbb{R}^{n\times 1} \text{and } \ \mathbf{v}_\mathrm{s} \in \mathbb{R}^{m\times 1} \tag{8}$$

where in this case,

$$\mathbf{d} = [d_x \, d_y \, d_z \, d_{\theta_x} \, d_{\theta_y}]^T, \tag{9}$$

and

$$\mathbf{v_s} = [v_{s_{xt+}} \, v_{s_{xb+}} \, v_{s_{xt-}} \, v_{s_{xb-}} \, v_{s_{yt+}} \, v_{s_{yb+}} \, v_{s_{yt-}} \, v_{s_{yb-}}]^\mathrm{T}. \tag{10}$$

Exciting the system one input at a time in full-range and recording the true displacement $\mathbf{d}$ and the sensor voltages $\mathbf{v_s}$ will result in measurement pairs

$$\begin{aligned} \mathbf{D} &= [\mathbf{d_1}, \mathbf{d_2}, \ldots, \mathbf{d_n}] \qquad &\mathbf{D} \in \mathbb{R}^{n\times n}, \\ \mathbf{V} &= [\mathbf{v_{s1}}, \mathbf{v_{s2}}, \ldots, \mathbf{v_{sm}}] \qquad &\mathbf{V} \in \mathbb{R}^{m\times n}. \end{aligned} \tag{11}$$

Note that as the data is recorded in full-range and under the assumption of a linear system, matrices $\mathbf{D}$ and $\mathbf{V}$ will contain all the required information regarding linear and angular displacements and the cross-coupling motions. The transformation matrix that maps the input displacements to the sensor voltages can be expressed as,

$$\mathbf{T}_\mathrm{s}\mathbf{D} = \mathbf{V}. \tag{12}$$

The matrix dimensions in equation (12) do not agree therefore the solution for $\mathbf{T_s}$ is not trivial. Vectorizing both sides of equation (12),

$$\mathrm{vec}(\mathbf{T}_\mathrm{s}\mathbf{D}) = \mathrm{vec}(\mathbf{V}), \tag{13}$$

the left-hand-side of equation (13) can be expressed by Kronecker product (Macedo and Oliveira (2013)) as,

$$\underbrace{(\mathbf{D^T} \otimes \mathbb{I}_\mathbf{m})}_{\mathrm{A}} \underbrace{\mathrm{vec}(\mathbf{T}_\mathrm{s})}_{\mathrm{x}} = \underbrace{\mathrm{vec}(\mathbf{V})}_{\mathrm{b}}. \tag{14}$$

This is a linear program $Ax = b$ with solution

$$x = (A^T A)^{-1} A^T b. \tag{15}$$

Solving for $x \in \mathbb{R}^{mn\times 1}$ and reshaping will give $\mathbf{T}_\mathrm{s} \in \mathbb{R}^{m\times n}$. The ideal outcome for the calibration process is to achieve identity when dividing the estimated matrix $\widehat{\mathbf{D}}$ by the true displacement matrix $\mathbf{D}$ as follow

$$N = \frac{\widehat{D}}{D} = \mathbb{I}_n. \tag{16}$$

4. EXPERIMENTAL SET-UP

The experimental set-up is shown in Fig. 6. The true translation and rotations, d_x,d_y d_z, θ_x and θ_y, were measured by an Attocube FPS3010 laser interferometer. The calibration process was implemented using a dSPACE DS1103 hardware system via Simulink Coder. The sensor voltages were read through a custom made flexible PCB circuit shown in Fig. 1. A custom circuit implementing the Jacobian matrix $\mathbf{J}$ was used to produce the eight electrode voltages. The stage was driven by an eight-channel high-voltage amplifier, where each channel has a gain of 25. The full operating range of the nanopositioner is from -200 V to $+500$ V. However, for safety reasons, a range of -200 V to $+200$ V was chosen.

5. CALIBRATION RESULTS

The experimental set-up shown in Fig. 6 is used for the data acquisition purposes. The sensor matrix $\mathbf{T_s}$ is identified following the process described in Section 3.3. Matrix $\mathbf{T_v}$ is already known and is given by equation (3), therefore the calibration matrix $\mathbf{T_c}$ can be identified from equation (7). The ideal outcome for the calibration process is to achieve identity in equation (16). The result of the calibration is shown below:

$$N = \frac{\widehat{D}}{D} = \begin{bmatrix} 1.0032 & 0.0110 & 0.0306 & 0.0075 & 0.0130 \\ 0.0360 & 1.0016 & 0.0167 & 0.0070 & 0.0126 \\ 0.0153 & 0.0007 & 1.0425 & 0.0014 & 0.0088 \\ 0.0031 & 0.0089 & 0.0012 & 1.0123 & 0.0018 \\ 0.4326 & 0.0416 & 0.2416 & 0.0405 & 0.9291 \end{bmatrix} \tag{17}$$

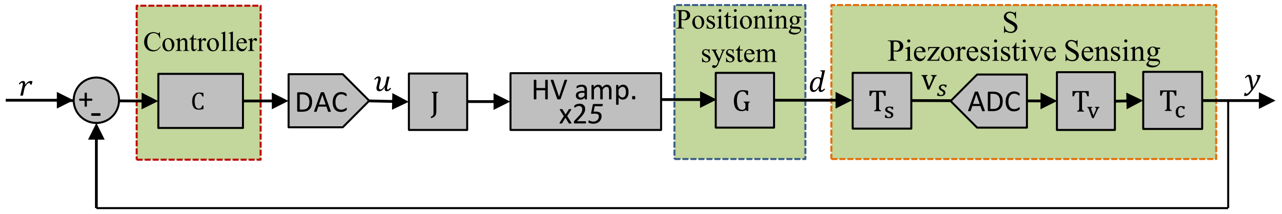

Fig. 7. The block diagram of the control law.

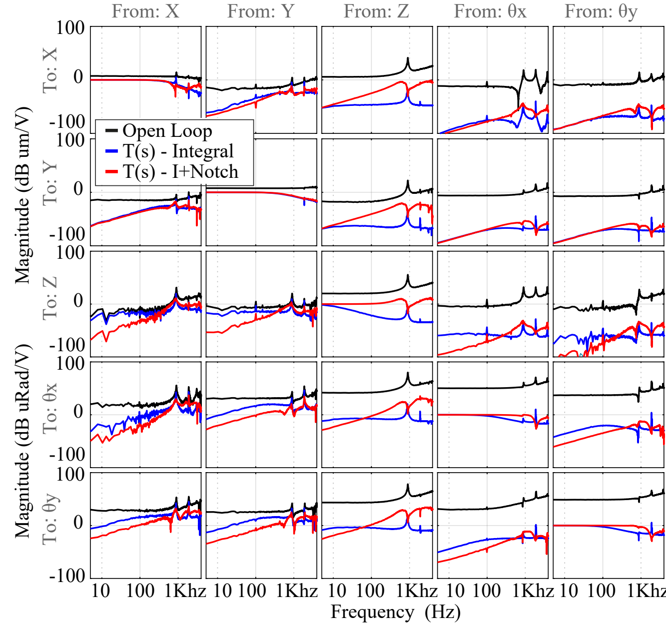

Fig. 8. The open-loop and closed-loop frequency responses.

It can be observed that the matrix N is close to identity with 1's in diagonal elements and 0's in off-diagonal elements; however, some residual cross-coupling can be observed in equation (17). These elements are not heavily weighted in the optimization due to their naturally low gain, and are not of practical concern.

6. DECENTRALIZED CONTROL

The performance of the proposed sensing design in closed-loop is evaluated by implementing a decentralized control law. For closed-loop control, a decentralized integral controller, and a decentralized integral and notch controller were implemented on a dSPACE-ds1103 board using Simulink coder. The vertical and rotational motions are measured using the proposed sensor. The block diagram of the control law is shown in Fig. 7 where C is a diagonal controller, G is the plant and S is the proposed sensor. The open-loop frequency response of the system measured by the sensor S is depicted in Fig. 8. The general diagonal controller for this system can be written as

$$C(s) = diag\{[c_1(s), c_2(s), c_3(s), c_4(s), c_5(s)]\} \tag{18}$$

where for the integral controller the transfer function of the diagonal elements are given by

$$c_i(s) = \frac{k_i}{s}, \quad i \in \{1, 2, \dots 5\}. \tag{19}$$

Each element in the diagonal controller $C(s)$ in equation (18) is designed based on the corresponding diagonal

Table 1. Controller Parameters

Controller	Para	X	Y	Z	θ_x	θ_y
I	k_i	1000	1000	5	-2	-3
I+Notch	k_i	1000	1000	400	-25	-25
	ζ_n	-	-	0.01	0.01	0.01
	ω_n (kHz)	-	-	0.9	1.88	1.88

element of $G(s)$ (Skogestad and Postlethwaite (2007)). The loop pairings have been chosen based on the frequency-dependent RGA with a diagonally dominant element RGA $= \Lambda = \mathbb{I}$ at frequencies of up to 1 kHz. With all loops closed, the overall response of the system to the reference input r can be written as

$$y = GC(I + GC)^{-1}r = Tr, \tag{20}$$

where T is the overall complementary sensitivity function. The complementary transfer function in loop i can be written as

$$T(i) = \frac{g_{ii}c_i}{1 + g_{ii}c_i}, \quad i \in \{1, 2, \dots 5\} \tag{21}$$

where g_{ii} is the i'th diagonal elements of plant G. To ensure the stability of the individual parts of the system, each loop is designed independently. The closed-loop stability in loop i is examined by the gain and phase margin of the loop transfer function $L_i = g_{ii}c_i$. The chosen integral gains are summarized in Table 1. The controllers are designed to maintain a gain and phase margin of at least 5 dB and 50°.

The open-loop and closed-loop frequency responses for each input-output pair of the 5×5 system are shown in Fig. 8. The open-loop frequency responses of the translational motions in the X and Y-axis exhibits a relatively constant response over a wide frequency range, therefore, a simple integral controller would be sufficient for in-plane motions. However, in out-of-plane, the maximum useful frequency is limited by the first and second resonant modes occurring at 900 Hz in the Z-axis and 1880 Hz in both θ_x and θ_y. To improve the bandwidth, notch filters are designed and tuned to the lowest resonance frequencies of the corresponding diagonal frequency responses. For translation in the Z-axis, the notch filter is tuned to 900 Hz and for rotations about the X and Y-axis, the filters are tuned to 1.88 kHz. The transfer function of the integral and notch controllers for the out-of-plane elements are given by

$$c_i(s) = \left(\frac{k_i}{s}\right) \frac{s^2 + 2\omega_n \zeta_n s + \omega_n^2}{(s + \omega_n)^2}, \quad i \in \{3, 4, 5\} \tag{22}$$

here ζ_n and ω_n are the damping ratio and the resonance frequency of the nanopositioner (Fleming and Leang (2014)) and k_i is the integral gain. For in-plane motions with $i \in \{1, 2\}$, the controllers will have the same gain and structure as equation (19). The controller parameters are summarized in Table 1. The closed-loop frequency

Table 2. Closed-loop Bandwidth

Controller		X	Y	Z	θ_x	θ_y
I	BW (Hz)	428	449	10	98	99
I+Notch	BW (Hz)	428	449	853	1450	1450

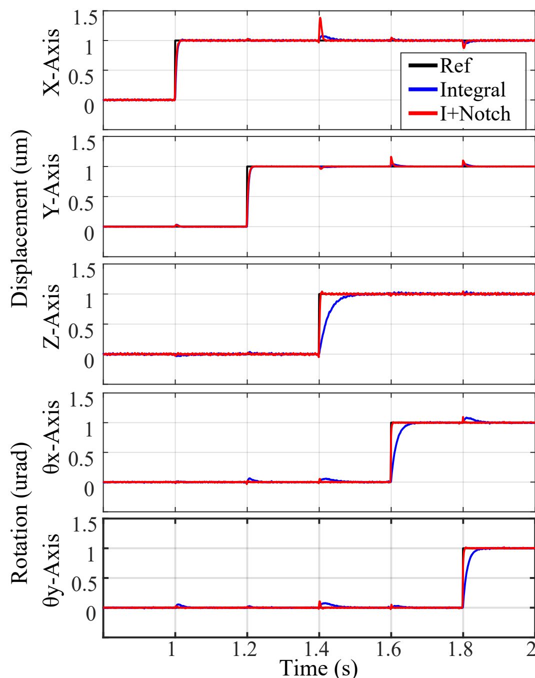

Fig. 9. The experimental closed-loop step responses.

responses are plotted in Fig. 8. The performance of the controllers in response to a step change is depicted in Fig. 9. The controller with the combined integrator and notch filter provides a better response than that of the integrator. The results also show a significant reduction in cross-coupling motions. The closed-loop performance of the system for each controller is summarized in Table. 2.

7. CONCLUSIONS

The article describes a new sensing design for linear and angular displacement measurements in multi-axis nanopositioning systems utilizing piezoresistive strain sensors. The proposed design employs system identification and feedforward techniques to provide decoupled measurements of linear and angular motions. The performance of the sensors in closed-loop is validated by implementing a decentralized controller. The experimental results show reference tracking in five-DOF using the proposed sensor.

REFERENCES

Anandan, N. and George, B. (2017). A wide-range capacitive sensor for linear and angular displacement measurement. *IEEE transactions on industrial electronics*, 64(7), 5728–5737.

Ekelof, S. (2001). The genesis of the wheatstone bridge. *Engineering Science & Education Journal*, 10(1), 37–40.

Fleming, A.J. and Leang, K.K. (2014). *Design, modeling and control of nanopositioning systems*. Springer.

Fleming, A.J. and Routley, B.S. (2015). A closed-loop phase-locked interferometer for wide bandwidth position sensing. *Review of Scientific Instruments*, 86(11), 115001.

Fleming, A.J. and Yong, Y.K. (2017). An ultrathin monolithic xy nanopositioning stage constructed from a single sheet of piezoelectric material. *IEEE/ASME Transactions on Mechatronics*, 22(6), 2611–2618.

Gates, B.D., Xu, Q., Love, J.C., Wolfe, D.B., and Whitesides, G.M. (2004). Unconventional nanofabrication. *Annu. Rev. Mater. Res.*, 34, 339–372.

Ghalehbeygi, O.T., Wills, A.G., Routley, B.S., and Fleming, A.J. (2017). Gradient-based optimization for efficient exposure planning in maskless lithography. *Journal of Micro/Nanolithography, MEMS, and MOEMS*, 16(3), 033507.

Macedo, H.D. and Oliveira, J.N. (2013). Typing linear algebra: A biproduct-oriented approach. *Science of Computer Programming*, 78(11), 2160–2191.

Moore, S.I., Fleming, A.J., and Yong, Y.K. (2019). Capacitive instrumentation and sensor fusion for high-bandwidth nanopositioning. *IEEE Sensors Letters*, 3(8), 1–3.

Moore, S.I., Omidbeike, M., Fleming, A., and Yong, Y.K. (2018). A monolithic serial-kinematic nanopositioner with integrated sensors and actuators. In *2018 IEEE/ASME International Conference on Advanced Intelligent Mechatronics (AIM)*, 150–155. IEEE.

Omidbeike, M., Yong, Y.K., Moore, S.I., and Fleming, A.J. (2019). A 5-axis monolithic nanopositioning stage constructed from a bimorph piezoelectric sheet. *International Conference on Manipulation, Automation and Robotics at Small Scales (MARSS)*.

Omidbeike, M., Routley, B., and Fleming, A.J. (2018). Independent estimation of temperature and strain in tee-rosette piezoresistive strain sensors. In *2018 IEEE/ASME International Conference on Advanced Intelligent Mechatronics (AIM)*, 131–135. IEEE.

Omidbeike, M., Teo, Y.R., Yong, Y.K., and Fleming, A.J. (2017). Tracking control of a monolithic piezoelectric nanopositioning stage using an integrated sensor. *IFAC-PapersOnLine*, 50(1), 10913–10917.

Ruppert, M.G., Moore, S.I., Zawierta, M., Fleming, A.J., Putrino, G., and Yong, Y.K. (2019). Multimodal atomic force microscopy with optimized higher eigenmode sensitivity using on-chip piezoelectric actuation and sensing. *Nanotechnology*, 30(8), 085503.

Skogestad, S. and Postlethwaite, I. (2007). *Multivariable feedback control: analysis and design*, volume 2. Wiley New York.

Sommargren, G.E. (1989). Linear and angular displacement measuring interferometer. US Patent 4,859,066.

Sun, L., Wang, J., Rong, W., Li, X., and Bao, H. (2008). A silicon integrated micro nano-positioning xy-stage for nano-manipulation. *Journal of Micromechanics and Microengineering*, 18(12), 125004.

Tortonese, M., Barrett, R., and Quate, C. (1993). Atomic resolution with an atomic force microscope using piezoresistive detection. *Applied physics letters*, 62(8), 834–836.